

HEART REGENERATION

Interplay between calcium and sarcomeres directs cardiomyocyte maturation during regeneration

Phong D. Nguyen^{1*}, Iris Gooijers^{1†}, Giulia Camprostrini^{2†}, Arie O. Verkerk^{3,4}, Hessel Honkoop¹, Mara Bouwman¹, Dennis E. M. de Bakker^{1,5}, Tim Koopmans^{1,6}, Aryan Vink⁷, Gerda E. M. Lamers⁸, Avraham Shakked⁹, Jonas Mars¹, Aat A. Mulder¹⁰, Sonja Chocron¹, Kerstin Bartscherer^{1,6}, Eldad Tzahor⁹, Christine L. Mummery², Teun P. de Boer¹¹, Milena Bellin^{2,12,13}, Jeroen Bakkers^{1,14*}

Zebrafish hearts can regenerate by replacing damaged tissue with new cardiomyocytes. Although the steps leading up to the proliferation of surviving cardiomyocytes have been extensively studied, little is known about the mechanisms that control proliferation and redifferentiation to a mature state. We found that the cardiac dyad, a structure that regulates calcium handling and excitation-contraction coupling, played a key role in the redifferentiation process. A component of the cardiac dyad called leucine-rich repeat-containing 10 (*Lrrc10*) acted as a negative regulator of proliferation, prevented cardiomegaly, and induced redifferentiation. We found that its function was conserved in mammalian cardiomyocytes. This study highlights the importance of the underlying mechanisms required for heart regeneration and their application to the generation of fully functional cardiomyocytes.

After a myocardial infarction (MI), the mammalian heart loses millions of cardiomyocytes (CMs) that are replaced by a permanent fibrotic scar. Inducing endogenous CM proliferation to replace the lost CMs is a promising strategy (1) that is observed after injury in zebrafish (2), salamanders (3), and embryonic or neonatal mammalian hearts (4–6). However, an underappreciated aspect of heart regeneration is the control of CM proliferation. Successful induction of CM proliferation (7–11) results in cardiomegaly (large heart) owing to uncontrolled CM proliferation despite positive regenerative outcomes. Furthermore, CM proliferation is preceded by CM dedifferentiation, which results in sarcomere breakdown, metabolic reprogramming, and reexpression of embryonic

genes (2, 12–18). If this dedifferentiated and proliferative state continues, long-term negative outcomes can reduce CM integration into the heart and decrease heart function (19–23).

The zebrafish has a natural regenerative capacity, which makes it an excellent model to investigate how CM proliferation and dedifferentiation-redifferentiation is controlled (2, 12–15, 24–26). However, little is known about the mechanisms that restore the injured heart to its original size and function.

Ca²⁺ handling of border-zone CMs changes during regeneration

CMs exhibit cycles of excitation-contraction (EC) coupling and Ca²⁺ handling (27, 28). During EC coupling, an influx of Ca²⁺ through L-type calcium channels (LTCCs) triggers Ca²⁺ release from the sarcoplasmic reticulum (SR). This results in sarcomere contraction, after which Ca²⁺ is shuttled back into the SR or out of the cell. Because Ca²⁺ handling changes as CMs mature, we developed an ex vivo imaging system using a transgenic zebrafish line that expressed the fluorescent Ca²⁺ sensor GCaMP6f (29) specifically in CMs to track the dynamics during regeneration (26) (Fig. 1, A to A').

Comparisons between CMs from the uninjured remote zone (RZ) and the border zone (BZ)—the region adjacent to the infarcted area, where CMs dedifferentiate and proliferate—showed differences in Ca²⁺ influx and efflux duration during the early regeneration time points, which were resolved by 21 days post-injury (dpi) (Fig. 1, B and C). There were no differences between trabecular and cortical BZ-CMs despite their reported different regenerative potential (25, 30) (fig. S1, A and A'). Next, we compared BZ-CM Ca²⁺ transients with embryonic CMs and found that although

Ca²⁺ influx was indistinguishable between time points (fig. S1B), there were significant differences in the Ca²⁺ efflux between embryonic and initial stages of regeneration compared with later regeneration stages (Fig. 1D). Thus, BZ-CMs functionally reverted to an embryonic-like state during the early regeneration stages in a time-dependent manner, which agrees with previous histological and transcriptomic observations (12, 13).

Lrrc10 marks the onset of CM maturation

We next used single-cell RNA sequencing (scRNA-seq) on BZ-CMs from early (7 dpi) and late (21 dpi) regeneration stages to more broadly characterize the process of redifferentiation and maturation (table S1). Initial analysis revealed that CMs clustered in a ring-like manner (Fig. 2A and fig. S2, A and A'), which mimicked a dedifferentiation-redifferentiation cycle when analyzed using CytoTrace (31) (Fig. 2B). To simplify downstream analysis, cells were projected into a linear pseudotime trajectory (32) to represent the regenerating CM axis (Fig. 2C and fig. S2, B to B'). In this axis, we determined the order of processes that CMs undergo during regeneration and broadly categorized this axis into an early and a late regeneration phase (Fig. 2D). The early regeneration phase showed high expression of genes related to injury, heart development, sarcomeres, cell cycle, glycolysis, and mitochondrial-related translation (Fig. 2D and fig. S2C), consistent with the previously identified CM dedifferentiation phase (2, 12–18, 24, 25, 33, 34). In the late regeneration phase, CMs progressed through states associated with CM maturity, such as Ca²⁺ regulation, mitochondrial oxidative phosphorylation (OXPHOS), cytoplasmic-related translation, and ion channels (Fig. 2D and fig. S2C').

Given that Ca²⁺ dynamics were different between early and late regeneration phases and that genes related to Ca²⁺ regulation were prominently expressed during the late regeneration phase, we searched for candidate genes that could potentially be involved in this state of the regenerating CM axis. An interpopulation analysis of Mexican cavefish, in which heart regeneration does not take place after injury, identified the leucine-rich repeat-containing 10 (*lrrc10*) gene—encoding an LTCC accessory protein (35, 36)—as a player in heart regeneration (37); yet, the underlying mechanism remains unknown. Specifically, *lrrc10* knockout zebrafish mutants retain a scar (37) (fig. S3, A and A') yet display normal BZ-CM proliferation (37). Notably, *lrrc10* was down-regulated in the early regeneration phase and up-regulated at the start of the late regeneration phase (Fig. 2D and fig. S2, C and C'), which was experimentally validated (fig. S4, A to G). Furthermore, comparisons between uninjured adult *lrrc10* siblings revealed no

¹Hubrecht Institute-KNAW and University Medical Center Utrecht, Utrecht, Netherlands. ²Department of Anatomy and Embryology, Leiden University Medical Center, Leiden, Netherlands. ³Department of Medical Biology, Amsterdam Cardiovascular Sciences, University of Amsterdam, Amsterdam University Medical Center, Amsterdam, Netherlands. ⁴Department of Experimental Cardiology, University of Amsterdam, Amsterdam University Medical Center, Amsterdam, Netherlands. ⁵Leibniz Institute on Aging – Fritz Lipmann Institute (FLI), Jena, Germany. ⁶Department of Animal Physiology, Osnabrueck University, Osnabrück, Germany. ⁷Department of Pathology, University Medical Center Utrecht, Utrecht University, Utrecht, Netherlands. ⁸Core Facility Microscopy, Institute of Biogly, Leiden University, Leiden, Netherlands. ⁹Department of Molecular Cell Biology, Weizmann Institute of Science, Rehovot, Israel. ¹⁰Department of Cell and Chemical Biology, Leiden University Medical Center, Leiden, Netherlands. ¹¹Department of Medical Physiology, Division of Heart and Lungs, University Medical Center Utrecht, Utrecht, Netherlands. ¹²Department of Biology, University of Padua, Padua, Italy. ¹³Veneto Institute of Molecular Medicine, Padua, Italy. ¹⁴Department of Pediatric Cardiology, Division of Pediatrics, University Medical Center Utrecht, Utrecht, Netherlands.

*Corresponding author. Email: p.nguyen@hubrecht.eu (P.D.N.); j.bakkers@hubrecht.eu (J.B.)

†These authors contributed equally to this work.

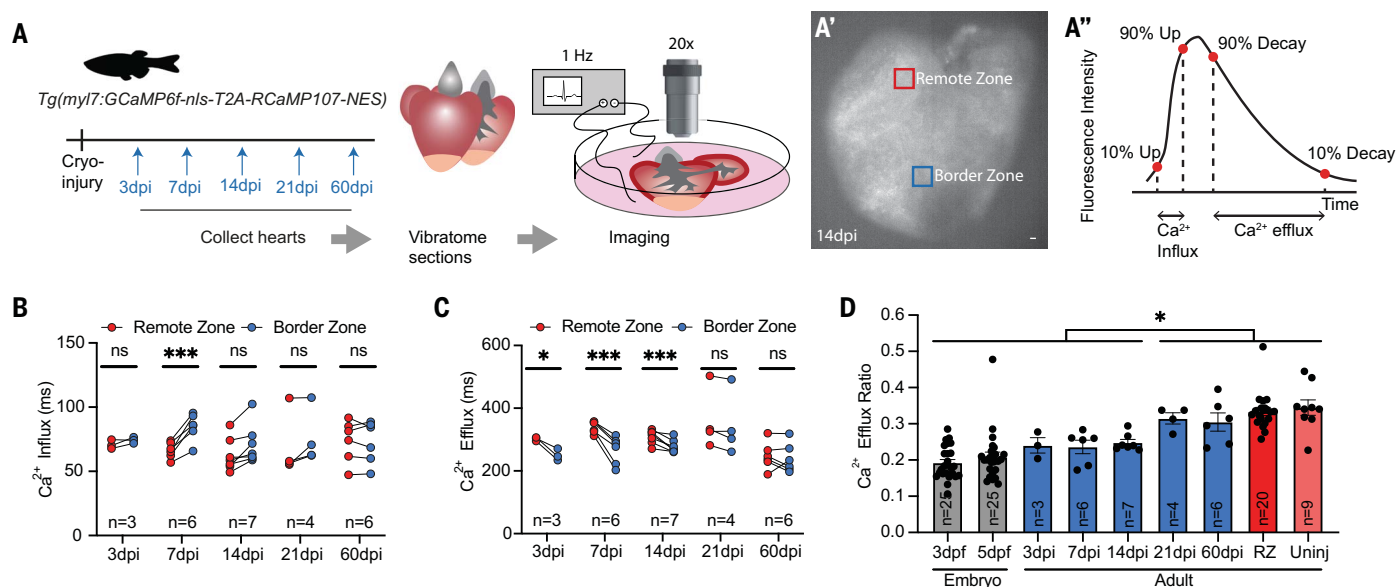


Fig. 1. Ca^{2+} handling matures in CMs during regeneration. (A' and A'') Strategy for monitoring live Ca^{2+} cycling in adult hearts. (A) Adult fish containing the Ca^{2+} sensors $\text{Tg}(myl7:\text{GCaMP6f-nls-T2A-RCaMP107-NES-pA})$ were injured. At a designated time point, cardiac slices were made and attached to electrodes for synchronous electrical stimulation, and the GCaMP signal was recorded at high speed ex vivo. (A') The fluorescence intensity changes over time in the RZ (red) and BZ (blue) were extracted from recordings. Scale bar, 100 μm . (A'') Example of the GCaMP peak whereby various characteristics of the curve were analyzed with custom MATLAB scripts. The difference in duration between 10% and 90% upstroke corresponded to Ca^{2+} influx. The difference in duration between 90% and 10% decay corresponded to Ca^{2+} efflux. (B) Quantification of Ca^{2+} influx of adult hearts after

injury reveals only a significant difference in Ca^{2+} handling between RZ- and BZ-CMs at 7 dpi. Paired t test was conducted. (C) Quantification of Ca^{2+} efflux of adult hearts after injury reveals that Ca^{2+} handling is different between RZ- and BZ-CMs during early stages of regeneration (3 dpi, 7 dpi, and 14 dpi) with a recovery from 21 dpi onward. Paired t test was conducted. (D) Quantification of Ca^{2+} efflux of both embryonic [3 days postfertilization (dpf) and 5 dpf] and adult (RZ and uninjured) hearts reveal that BZ-CMs at early regeneration stages (3 dpi, 7 dpi, and 14 dpi) functionally resemble embryonic CMs, whereas they resemble adult CMs at late (21 dpi and 60 dpi) regeneration stages. One-way analysis of variance (ANOVA) was conducted. Throughout the figures, P values are as follows: * $P < 0.05$; ** $P < 0.01$; *** $P < 0.001$; **** $P < 0.0001$; ns, not significant.

differences in Ca^{2+} influx; however, Ca^{2+} efflux was prolonged (fig. S3B). During regeneration, *lrrc10*^{-/-} CMs failed to recover both their Ca^{2+} influx and efflux at the early (7 dpi) and even at the late regeneration stages (21 dpi and 60 dpi) (Fig. 2, E to F, and fig. S3C). Moreover, *lrrc10*^{-/-} BZ-CMs functionally maintained an embryonic Ca^{2+} handling phenotype even at the late regeneration stage (60 dpi), indicating that they failed to redifferentiate (Fig. 2G and fig. S3D). These results suggest a role for *Lrrc10* during CM maturation. Corroborating this model, the expression of *lrrc10* in BZ-CMs negatively correlated with the expression of dedifferentiation markers (embryonic MYH and pS6) (Fig. 2, H and I, and fig. S5, A and A'). Additionally, expression of dedifferentiation markers (*myomesin*, *hexokinase1*, and pS6) reverted to normal levels in *lrrc10*^{+/+} hearts at the late regeneration time point (21 dpi), whereas these markers remained elevated in *lrrc10*^{-/-} BZ-CMs (Fig. 2, I and I', and fig. S5, B to C''). By contrast, *Lrrc10* overexpression (OE) at the early regeneration time point (7 dpi) eliminated pS6 expression specifically in BZ-CMs (fig. S5, D and D'). Thus, *Lrrc10* plays a critical role in actively maturing CMs by inhibiting early regeneration hallmarks, whereas *lrrc10* mutants appeared to

be perpetually held in an early regeneration phase and consequently failed to regenerate.

LRRC10 OE can induce maturation in human-induced pluripotent stem cell (hiPSC)-CMs

Human patients and mice harboring homozygous loss-of-function mutations in *LRRC10* and *Lrrc10*, respectively, develop dilated cardiomyopathy (35, 38, 39). To test whether LRRC10 could also induce CM maturation in humans, we used hiPSC-CMs because they resemble fetal CMs (28, 40). hiPSC-CMs with LRRC10 OE displayed significantly improved sarcomere organization and sarcomere length (Fig. 3, A to A'). Furthermore, we observed a significant increase in LTCC ($\text{Ca}_v1.2$) expression after LRRC10 OE (Fig. 3, B and B') as well as increased connexin-43 (CX43) expression and localization between neighboring CMs (fig. S6, A to B'). Given the increase in an LTCC component as well as intracellular coupling, Ca^{2+} transients of hiPSC-CM cultures were measured. Both Ca^{2+} influx and efflux duration showed a significant increase in cultures with LRRC10 OE (fig. S6C), mirroring the dynamics seen in three-dimensional (3D) hiPSC cardiac microtissues, which display a mature CM state (40) (fig. S6D). Moreover, LRRC10 OE CM cultures had significantly more trans-

verse tubules (t-tubules) compared with the immature hiPSC-CMs (fig. S6, E and E').

To assess whether LRRC10 OE induced a broader maturation signature, we analyzed transcription profiles by scRNA-seq. We identified six distinct clusters, and application of CytoTrace (31) and pseudotime trajectory analysis to determine the maturation axis showed that hiPSC-CM maturation correlated with LRRC10 expression levels (Fig. 3, C to E; fig. S7, A to B'; and table S1). We performed further examination of the maturation status using markers such as sarcomeric isoform switching (Fig. 3F and fig. S7C), metabolic state switching (Fig. 3G), expression of EC coupling markers (fig. S7D), and comparison with expression profiles of hiPSC-CMs matured in a 3D microtissue format (fig. S7E). Overall, we found that the expression of LRRC10 is not associated with the end of maturation, but rather the onset of its expression appears to advance progression of hiPSC-CMs to a more mature state.

The cardiac dyad is disrupted after injury and requires *Lrrc10* to reassemble

The cardiac dyad is a region that assists in efficient EC coupling by placing components that regulate Ca^{2+} flux (LTCC complex and SR) and sarcomeres in proximity. Because *Lrrc10*

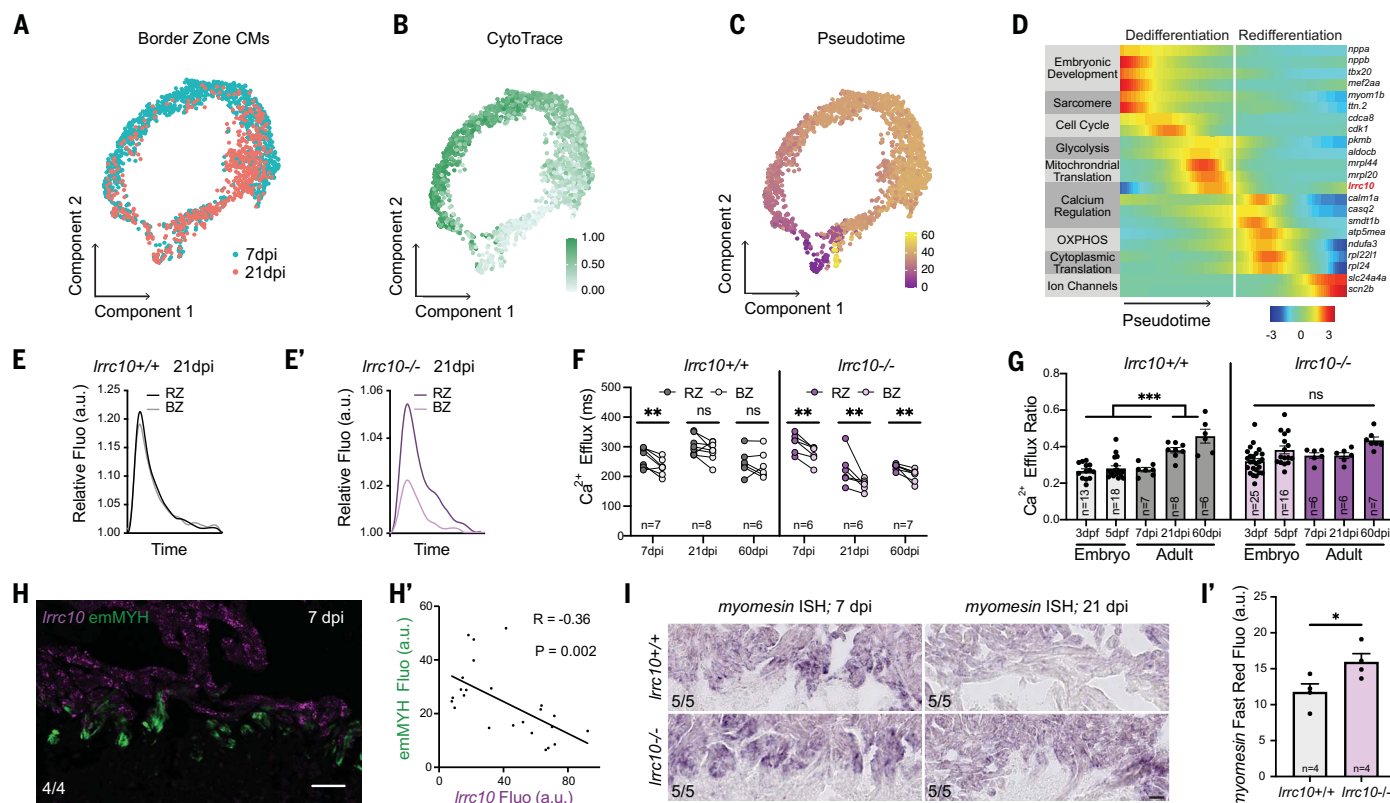


Fig. 2. Ca^{2+} handling maturation requires *Ircc10*. (A) Uniform manifold approximation and projection (UMAP) representation of the scRNA-seq data obtained from 7 dpi and 21 dpi BZ-CMs. (B) UMAP representation of scaled CytoTrace scores, which indicates the extent of differentiation. A value of 0 (white) is the most differentiated, and a value of 1 (green) is the least differentiated. (C) UMAP representation of linear pseudotime trajectory. A value of 0 (purple) indicates the start of pseudotime, whereas a value of 60 (yellow) indicates the end of pseudotime. (D) Heatmaps of gene expression that are grouped into processes across pseudotime. The red gene is *Ircc10*, and the white horizontal line represents the split between the de- and redifferentiation phases. (E) Relative GCaMP fluorescence intensity profile of *Ircc10*^{+/+} in RZ- and BZ-CMs at 21 dpi. a.u., arbitrary units. (E') Relative GCaMP fluorescence intensity profile of *Ircc10*^{-/-} in RZ- and BZ-CMs at 21 dpi. (F) Quantification of Ca^{2+} efflux in *Ircc10*^{+/+} and *Ircc10*^{-/-} at an early regeneration

time point, 7 dpi, and late regeneration time points of 21 dpi and 60 dpi. Paired *t* test was conducted. (G) Quantification of the Ca^{2+} efflux in embryonic and adult CMs in *Ircc10* siblings reveals that *Ircc10*^{-/-} functionally resemble embryonic CMs. One-way ANOVA was conducted. (H) RNAscope with *Ircc10* probe (purple) and embryonic myosin (emMYH) antibody (green) at the BZ at 7 dpi. Number indicates biological replicates, and the scale bar is 50 μm . (H') Quantification of *Ircc10* RNAscope (x axis, purple) and emMYH (y axis, green) signals reveal a negative correlation of the fluorescence intensity. *R* is the R^2 value, and *P* is the *P* value. (I) In situ hybridization with *myomesin* probe marking BZ-CM expression at 7 dpi in *Ircc10*^{+/+} and *Ircc10*^{-/-}. Number represents biological replicates, and the scale bar is 100 μm . (I') Quantification of FastRed *myomesin* signal at 21 dpi reveals significantly higher expression in *Ircc10*^{-/-} BZ-CMs. Number represents biological replicates, and a *t* test was conducted.

associates with the LTCC complex (35, 36), we conducted patch-clamp measurements on isolated *Ircc10* wild-type and mutant adult zebrafish CMs to examine whether the aberrant Ca^{2+} transient behavior could be explained by altered LTCC-generated current ($I_{\text{Ca,L}}$) properties. These experiments indicated a decrease in $I_{\text{Ca,L}}$ density (Fig. 4A), which may have resulted in a smaller influx of Ca^{2+} ions through $I_{\text{Ca,L}}$ channels. However, this was counteracted by incomplete activation and Ca^{2+} -dependent facilitation (41) (Fig. 4A') and prolonged $I_{\text{Ca,L}}$ (Fig. 4A''), ultimately resulting in action potential prolongation (fig. S8, A to A''). These effects presumably reflected the downstream *Ircc10*-dependent Ca^{2+} handling dynamics.

Mammalian LRRC10 colocalizes with dyad components, such as α -actinin (39, 42, 43), RyR2 (43), and junctophilin 2 (36), and binds

to sarcomeres via α -actinin (39, 42, 43) and the LTCC complex via $\text{Ca}_v1.2$ (35). Because it is unclear whether a zebrafish cardiac dyad exists, we investigated the localization of its components in uninjured adult CMs. All the dyad components, in addition to green fluorescent protein (GFP)-*Ircc10* were coexpressed and localized to the z-disc (Fig. 4B and fig. S8, B to B''), thereby identifying the zebrafish equivalent cardiac dyad. We next examined the distributions of these dyad components in *Ircc10* siblings. As expected, uninjured *Ircc10*^{+/+} CMs showed clear colocalization of the dyad components (fig. S8C). However, although uninjured *Ircc10*^{-/-} CMs displayed comparable localization of sarcomeres (α -actinin), the LTCC complex ($\text{Ca}_v1.2$) appeared disorganized (fig. S8C'), further complementing the Ca^{2+} flux and patch-clamp data. In the context of re-

generation, both *Ircc10* wild-type and mutant siblings displayed disorganization of both α -actinin and $\text{Ca}_v1.2$ at the early regeneration time point, 7 dpi (Fig. 4C). At later regeneration time points (21 dpi and 60 dpi), and supporting the Ca^{2+} flux analysis, *Ircc10*^{+/+} BZ-CMs had reorganized their dyad components such that they were comparable to those of uninjured hearts. On the other hand, although *Ircc10*^{-/-} BZ-CMs at 21 dpi and 60 dpi showed sarcomere reorganization, they failed to relocalize $\text{Ca}_v1.2$ to the z-disc (Fig. 4D and fig. S8, D and D'). We next investigated whether the disorganization of the cardiac dyad after injury was also observed in mammals. In MI-injured mouse hearts, BZ-CMs adjacent to the scar showed a complete disorganization of the dyad at both early and late time points (Fig. 4, E and F, and fig. S9, A to B'), and

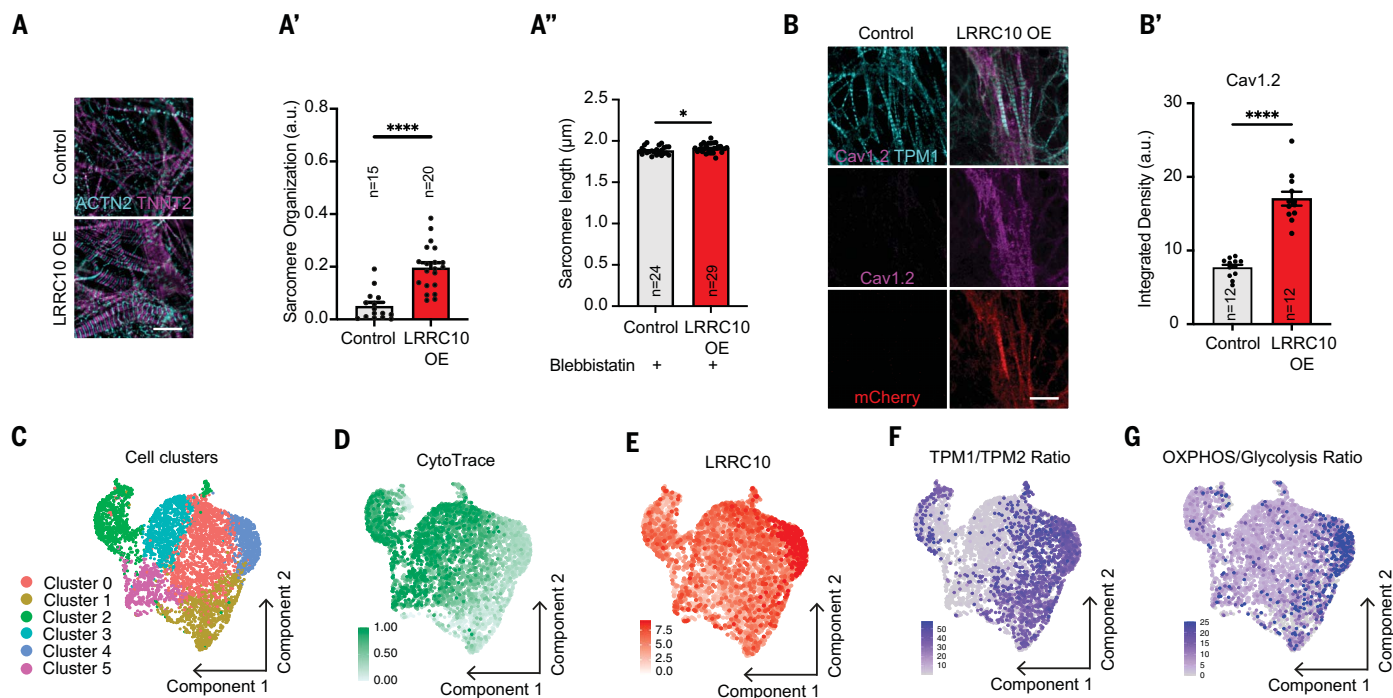


Fig. 3. LRRC10 drives hiPSC-CM maturation. (A) Immunostaining with ACTN2 to mark z-disc (cyan) and TNNT2 to mark sarcomeres (magenta) reveals typical disorganized sarcomeres indicating immature iPSC-CMs in the control group and fully assembled sarcomeres in the transfected LRRC10 OE group. Scale bar, 10 μ m. (A') Quantification of sarcomere organization in (A) reveals a significant increase after LRRC10 OE compared with control. *t* test was used, and numbers indicate biological replicates. (A'') Quantification of sarcomere length in (A) reveals a significant increase after LRRC10 OE compared with control. *t* test was conducted, and numbers indicate biological replicates. (B) Immunostaining with mCherry to mark transfected LRRC10 OE, TPM1 to mark z-disc (cyan), and Cav1.2 to mark LTCC (magenta) reveals highly disorganized dyads, indicating immature hiPSC-CMs in the control group and assembled dyads in

the LRRC10 OE group. Scale bar, 10 μ m. (B') Quantification of Cav1.2 signal in (B) reveals a significant increase in fluorescence only in the LRRC10 OE group. *t* test was conducted, and numbers indicate biological replicates. (C) UMAP representation of LRRC10 transfected hiPSC-CMs identifies six clusters in the scRNA-seq dataset. (D) UMAP representation of scaled CytoTrace scores which indicates the extent of differentiation. A value of 0 (white) is the most differentiated, and a value of 1 (green) is the least differentiated. (E) UMAP representation of LRRC10 expression indicates highest expression in cluster 4. (F) UMAP representation of TPM1/TPM2 ratio, which represents a sarcomere isoform switch from TPM2 to TPM1, is observed in the maturation axis. (G) UMAP representation of OXPHOS/glycolysis ratio, which represents a metabolic switch from expression of glycolytic genes to OXPHOS genes, is observed in the maturation axis.

Lrrc10 expression was significantly reduced in BZ-CMs (fig. S9, C and C'). Similarly, RZ-CMs in a human MI heart showed fully assembled cardiac dyad components located at the z-disc, whereas BZ-CMs located in the recent and old MI regions displayed completely disorganized cardiac dyads (Fig. 4G and fig. S10, A to E'').

Because the cardiac dyad is affected during injury and *lrrc10* may be implicated in its assembly, we next examined how *lrrc10* was driving these dynamics. Transmission electron microscopy on uninjured *lrrc10* sibling hearts revealed that the proteins at the z-disc in *lrrc10*^{-/-} were not as tightly localized to the z-disc as seen in *lrrc10*^{+/+} (fig. S11, A and A'). We noted that *lrrc10*^{-/-} CMs lacked structures that resembled caveolae (fig. S11B). Next, we examined *lrrc10* in a gain-of-function heart. Complete organization of sarcomeres in BZ-CMs at 7 dpi were observed when disorganized or disassembled sarcomeres should have normally been present (fig. S5, D and D', and

fig. S11C). Furthermore, we found relocalization of Cav1.2 to the dyad region in early regenerating BZ-CMs (7 dpi) (fig. S11C), which would normally be disorganized at this stage in wild-type CMs (Fig. 4D). Thus, *Lrrc10* helps to drive the assembly of the cardiac dyad at the z-disc.

Knockdown of *tnnt2a* by antisense morpholino injections impairs sarcomere assembly (44). In this case, the sarcomere itself is not assembled properly, but all the sarcomeric components are still present, which provides a condition to test whether *Lrrc10* was actively involved in sarcomere reassembly. Although we did not see full rescue of sarcomere assembly in GFP-*Lrrc10*-overexpressing hearts in the presence of the *tnnt2a* morpholino, we observed increased puncta staining at a higher fluorescence intensity in sarcomeres (fig. S12, A to Diii'). This suggested that the presence of *Lrrc10* could direct the cardiac dyad to localize to the z-disc. We tested this directly with fluorescent recovery after photobleaching (FRAP) of Cav1.2-mCherry and Actn2-mCherry in the

presence or absence of GFP-*Lrrc10*. The presence of ectopic GFP-*Lrrc10* increased the amount of α -actinin and Cav1.2 returning to the bleached region of interest (fig. S13, A to C). Thus, *Lrrc10* actively drives the reassembly of the cardiac dyad.

Lrrc10 inhibits CM proliferation and can prevent cardiomegaly

CM proliferation is a hallmark of the early regeneration phase, and peak proliferation occurs at 7 dpi (14, 26, 33), which coincides with the transient peak in *lrrc10* expression (Fig. 2D and fig. S4, A to G). This high *lrrc10* expression negatively correlated with EdU incorporation, a marker of cell proliferation (fig. S14, A and A'). To investigate whether CMs with high *lrrc10* expression had undergone a round of cell cycle activation at an earlier stage, we performed double-pulse chase experiments with an early EdU pulse at 6 dpi followed by a late BrdU pulse at 8 dpi. The high expression of *lrrc10* was associated with EdU⁺/BrdU⁻ CMs but

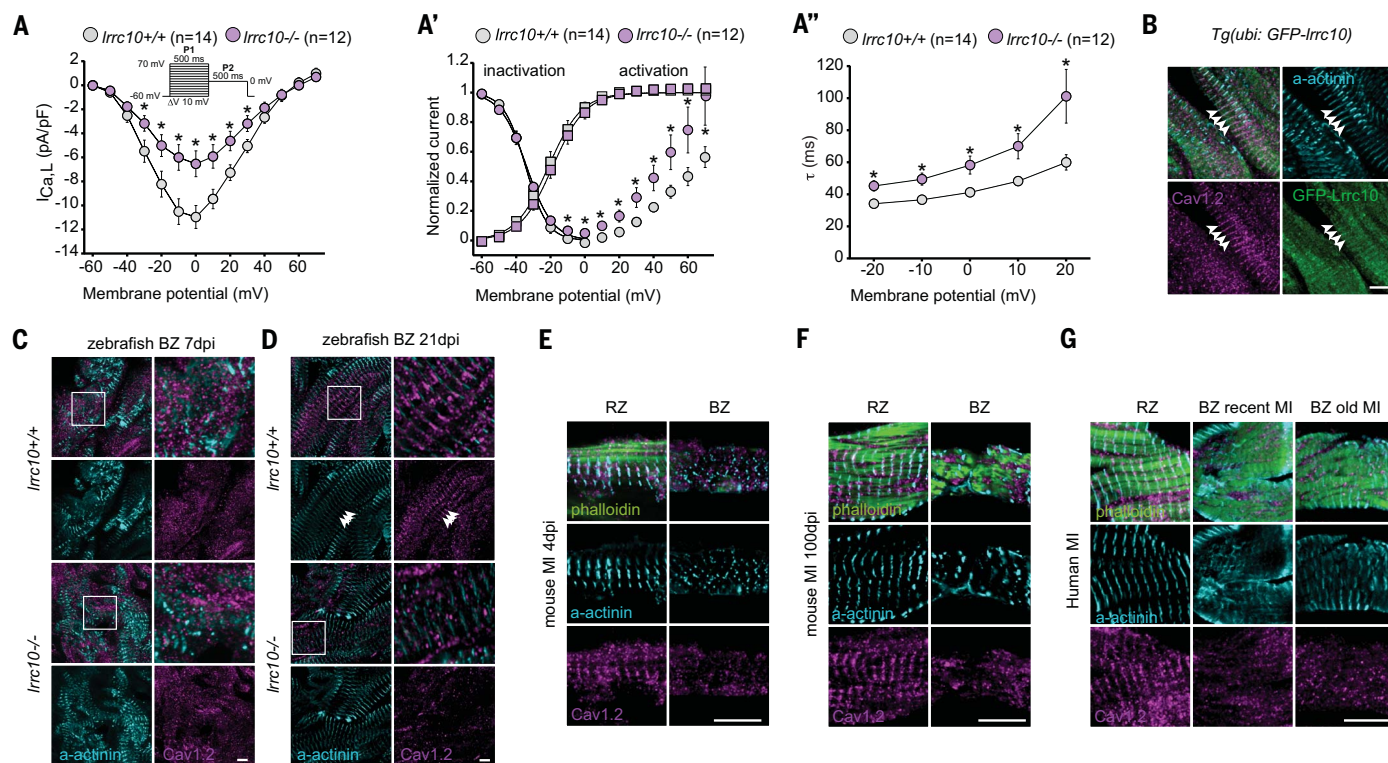


Fig. 4. *Lrrc10* is required for cardiac dyad formation during regeneration.

(A) Patch clamp on isolated uninjured adult CMs reveals a lower current density in *lrrc10*^{-/-} CMs when measuring average current-voltage of I_{CaL} current. WT, wild-type. (A') Patch clamp on isolated uninjured adult CMs reveals that *lrrc10*^{-/-} CMs cannot inactivate and have a larger repolarization phase, resulting in more current when measuring voltage dependency of inactivation and activation of I_{CaL} current. Activation was not different. Circles represent inactivation, and squares represent activation. (A'') Speed (τ) of I_{CaL} inactivation of patch clamped-isolated uninjured adult CMs. (B) Antibody staining in *Tg(ubi:GFP-Lrrc10)* uninjured hearts with α -actinin to mark the z-disc (cyan), $Ca_v1.2$ to mark LTCC (magenta), and GFP to mark the localization of the GFP-Lrrc10 fusion protein (green). Arrowheads denote examples of colocalization. Scale bar, 100 μ m. (C) Antibody staining at 7 dpi in *lrrc10*^{+/+} and *lrrc10*^{-/-} hearts with α -actinin to mark the z-disc (cyan) and $Ca_v1.2$

to mark LTCC (magenta) reveal disorganized dyads. Scale bar, 100 μ m. (D) Antibody staining at 21 dpi with α -actinin (cyan) and $Ca_v1.2$ (magenta) reveals reassembled dyads (arrowheads) in *lrrc10*^{+/+} but not in *lrrc10*^{-/-} hearts. Scale bar, 100 μ m. (E) Antibody staining of mouse MI at 4 dpi with phalloidin to mark CMs (green), α -actinin to mark the z-disc (cyan), and $Ca_v1.2$ to mark LTCC (magenta) reveals assembled dyads only in RM-CMs. Images represent four biological replicates. Scale bar, 10 μ m. (F) Antibody staining of mouse MI at 100 dpi with phalloidin to mark CMs (green), α -actinin to mark the z-disc (cyan), and $Ca_v1.2$ to mark LTCC (magenta) reveals that the BZ-CMs retain disorganized dyads. Images represent four biological replicates. Scale bar, 10 μ m. (G) Antibody staining in human MI with phalloidin to mark CMs (green), α -actinin to mark the z-disc (cyan), and $Ca_v1.2$ to mark LTCC (magenta) reveals assembled dyads in RM-CMs but not in BZ-CMs at recent and old MI regions. Image represents one replicate. Scale bar, 10 μ m.

not with EdU-/BrdU+ CMs (Fig. 5, A and A'), which suggests that *lrrc10* up-regulation is associated with the completion of proliferation and the onset of CM maturation. When examining CM proliferation at the late regeneration stage (21 dpi), there was significant maintenance of proliferation in *lrrc10*^{-/-} BZ-CMs, whereas at the early regeneration phase, *lrrc10*^{-/-} had comparable proliferation rates compared with their wild-type siblings (37) (Fig. 5B). Furthermore, *Lrrc10* OE caused a decrease in proliferation at the peak CM proliferation time point (7 dpi) (Fig. 5B). Thus, *lrrc10* is a negative regulator of proliferation and an initiator of CM maturity.

We next tested whether the negative correlation of *lrrc10* with proliferation was conserved in mammalian CMs. CM-specific OE of a constitutively active form of the ErbB2 (caErbB2) receptor induces CM dedifferentiation and pro-

liferation resulting in cardiomegaly (8). We observed that *LRRC10* OE was sufficient to decrease cell cycle activity in caErbB2 CMs (Fig. 5, C and C', and fig. S15, A to C). Moreover, examination of the cardiac dyad showed a significant increase in $Ca_v1.2$ expression but no obvious differences in sarcomere organization upon GFP-*LRRC10* OE (fig. S15, D to G). CM proliferation was also examined in hiPSC-CMs that overexpressed *LRRC10*. *LRRC10* OE caused a decrease in EdU incorporation (fig. S15H), pH3 (Fig. 5, D and D'), and a slower growth rate (fig. S15I). Thus, *lrrc10* plays a conserved role in halting CM proliferation across species.

Previous studies in mammals and zebrafish have provided methods to induce CM proliferation by activating specific genes and signaling pathways and have demonstrated positive regenerative outcomes after heart injury (7, 8, 11, 45, 46). A consequence of this un-

controlled CM proliferation, however, is the appearance of large hearts (cardiomegaly). We tested whether the inhibitory effects of *Lrrc10* on CM proliferation could prevent cardiomegaly. Continuous 6-week OE of a constitutively active form of vitamin D receptor A (ca-VdRA) (45) specifically in CMs resulted in enlarged hearts and visible bulging of the thoracic cavity owing to its excessive size. Notably, ca-VdRA fish coexpressing GFP-*Lrrc10* did not show signs of cardiomegaly (Fig. 5, E and E'). To more directly test whether the observed effect was the result of the inhibition of dedifferentiation and proliferation by *Lrrc10*, we used a vitamin D analog alfacalcidol in adult fish (45). Daily injections of alfacalcidol resulted in a significant increase in total ventricle volume in the wild-type group, whereas similar alfacalcidol injections in the GFP-*Lrrc10* fish line did not affect total ventricle volume (fig. S16, A

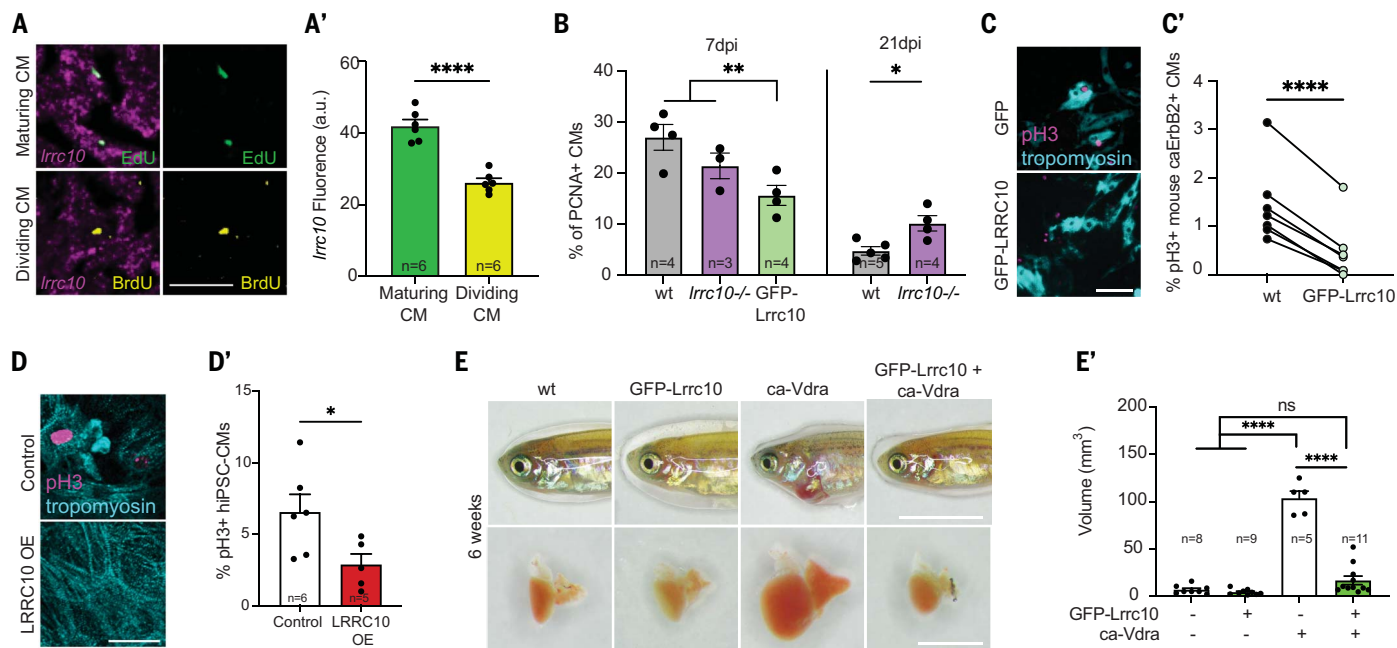


Fig. 5. *Lrrc10* inhibits CM proliferation and prevents cardiomegaly.

(A) RNAscope with *Lrrc10* probe (purple) in combination with a maturing CM (EdU+/BrdU-; green) and dividing CM (EdU-/BrdU+; yellow) in 7 dpi BZ-CM. Scale bar, 50 μ m. (A') Quantification of *Lrrc10* fluorescence signal reveals a negative correlation to proliferation and high *Lrrc10* expression. *t* test was conducted, and number indicates biological replicates. (B) Cell counting of PCNA⁺ BZ-CMs reveals similar proliferation level in *Lrrc10* siblings at 7 dpi and significantly high level in *Lrrc10*^{-/-} BZ-CMs at 21 dpi. *Lrrc10* OE causes a significant reduction of proliferation at 7 dpi. *t* test was conducted. (C) Antibody staining of mouse caErbB2⁺ CMs in control GFP only and GFP-LRRC10 OE

with proliferation (pH3; magenta) and tropomyosin to mark CMs (cyan). Scale bar, 150 μ m. (C') Quantification of proliferation of mouse caErbB2⁺ CMs after GFP-LRRC10 OE. Paired *t* test was conducted. (D) Antibody staining of hiPSC-CMs in control and LRRC10 OE with pH3 to mark proliferation (magenta) and tropomyosin to mark CMs (cyan). Scale bar, 50 μ m. (D') Quantification of proliferation in hiPSC-CMs after LRRC10 OE. *t* test was performed, and number represents biological replicates. (E) Images of fish and their hearts reveal that wild-type and GFP-LRRC10 OE fish have comparably sized hearts. ca-Vdra OE shows cardiomegaly, which is rescued when fish coexpress *Lrrc10*. Scale bar, 2 mm. (E') Quantification of heart volume. One-way ANOVA was conducted, and number represents biological replicates.

to C"). We confirmed that the increase in size was because of proliferation (fig. S16, A to C"). Finally, we tested whether *Lrrc10* could prevent cardiomegaly after CM-specific OE of neuregulin1 (*Nrg1*) (7). Control siblings and GFP-*Lrrc10* fish receiving phosphate-buffered saline (PBS) displayed normal hearts. Tamoxifen-induced recombined fish that overexpressed *Nrg1* displayed an exceptionally large heart. Meanwhile, GFP-*Lrrc10* fish that also overexpressed *Nrg1* did not show evidence of cardiomegaly (fig. S16, D to E'). Thus, *Lrrc10* inhibits CM proliferation, and its OE can robustly prevent cardiomegaly.

Discussion

CM proliferation has been the focus of intense research given its potential to generate new tissue for regeneration. However, although increasing CM numbers is important, the control and subsequent redifferentiation into mature CMs and the integration of these de novo CMs into the native heart is equally essential (22). This study provides evidence that rather than being a passive event, CM maturation is an active process. By broadly defining the regenerating CM axis after injury, we propose a mechanism whereby CMs normally use *Lrrc10*

to bind and recruit components of the sarcomere and LTCC to the cardiac dyad region located at the z-disc. After injury, a down-regulation of *Lrrc10* permits dedifferentiation of BZ-CMs at a transcriptional and functional level, leading to CM proliferation. Newly generated CMs then up-regulate *Lrrc10* to halt the early phase of regeneration and allow CMs to progress through the late regeneration phase, where *Lrrc10* aids the reassembly of the cardiac dyad and consequently facilitates the reformation of fully functioning mature CMs. The absence of *Lrrc10* leads to incomplete cardiac dyad reassembly and aberrant Ca²⁺ handling and causes CMs to remain in an early regenerative stage, thereby hampering complete regeneration. How exactly *Lrrc10* controls Ca²⁺ dynamics and whether regulating Ca²⁺ transients could modulate regeneration need to be further investigated.

Efficient communication between and within individual CMs permits synchronous contraction to produce maximum cardiac output. This remains an unresolved limiting factor for developing cellular-based therapies for heart failure. Specifically, exogenous cardiac tissue in which CM maturity has not been properly achieved fails to integrate with the preexisting

myocardium and exhibits asynchronous contractions; consequently, the long-term contribution to cardiac output is varied (19–23). This study shows the complex and highly interlinked interaction between sarcomere and Ca²⁺ regulation during CM maturation by using a cardiac regeneration model that naturally generates new CMs. We also found that this link holds true for mammalian CM maturation. We showed that the cardiac dyad is vital for this maturation process, which may provide a potential target to promote CM maturation.

REFERENCES AND NOTES

1. E. Tzahor, K. D. Poss, *Science* **356**, 1035–1039 (2017).
2. K. D. Poss, L. G. Wilson, M. T. Keating, *Science* **298**, 2188–2190 (2002).
3. J. W. Godwin, R. Debuque, E. Salimova, N. A. Rosenthal, *NPJ Regen. Med.* **2**, 22 (2017).
4. E. R. Porrello et al., *Science* **331**, 1078–1080 (2011).
5. E. R. Porrello et al., *Proc. Natl. Acad. Sci. U.S.A.* **110**, 187–192 (2013).
6. M. Notari et al., *Sci. Adv.* **4**, eaao5553 (2018).
7. M. Gemberling, R. Karra, A. L. Dickson, K. D. Poss, *eLife* **4**, e05871 (2015).
8. G. D'Uva et al., *Nat. Cell Biol.* **17**, 627–638 (2015).
9. A. Aharonov et al., *Nat. Cell Biol.* **22**, 1346–1356 (2020).
10. T. O. Monroe et al., *Dev. Cell* **48**, 765–779.e7 (2019).
11. M. Xin et al., *Proc. Natl. Acad. Sci. U.S.A.* **110**, 13839–13844 (2013).
12. H. Honkoop et al., *eLife* **8**, e50163 (2019).
13. K. Kikuchi et al., *Nature* **464**, 601–605 (2010).

14. F. Chablais, J. Veit, G. Rainer, A. Jaźwińska, *BMC Dev. Biol.* **11**, 21 (2011).
15. C. C. Wu *et al.*, *Dev. Cell* **36**, 36–49 (2016).
16. R. Fukuda *et al.*, *EMBO Rep.* **21**, e49752 (2020).
17. A. Beisaw *et al.*, *Circ. Res.* **126**, 1760–1778 (2020).
18. A. Lepilina *et al.*, *Cell* **127**, 607–619 (2006).
19. Y.-W. Liu *et al.*, *Nat. Biotechnol.* **36**, 597–605 (2018).
20. J. J. Chong *et al.*, *Nature* **510**, 273–277 (2014).
21. Y. Shiba *et al.*, *Nature* **538**, 388–391 (2016).
22. A. Shakked *et al.*, *Nat. Cardiovasc. Res.* **2**, 383–398 (2023).
23. K. Gabisonia *et al.*, *Nature* **569**, 418–422 (2019).
24. C. Jopling *et al.*, *Nature* **464**, 606–609 (2010).
25. V. Gupta, K. D. Poss, *Nature* **484**, 479–484 (2012).
26. A. Bertozzi *et al.*, *Dev. Biol.* **471**, 106–118 (2021).
27. D. A. Eisner, J. L. Caldwell, K. Kistamás, A. W. Trafford, *Circ. Res.* **121**, 181–195 (2017).
28. R. E. Ahmed, T. Anzai, N. Chanthra, H. Uosaki, *Front. Cell Dev. Biol.* **8**, 178–178 (2020).
29. T. W. Chen *et al.*, *Nature* **499**, 295–300 (2013).
30. H. Sánchez-Iranzo *et al.*, *Nat. Commun.* **9**, 428 (2018).
31. G. S. Gulati *et al.*, *Science* **367**, 405–411 (2020).
32. X. Qiu *et al.*, *Nat. Methods* **14**, 979–982 (2017).
33. J. M. González-Rosa, V. Martín, M. Peralta, M. Torres, N. Mercader, *Development* **138**, 1663–1674 (2011).
34. K. Schnabel, C. C. Wu, T. Kurth, G. Weidinger, *PLOS ONE* **6**, e18503 (2011).
35. M. T. Woon *et al.*, *J. Am. Heart Assoc.* **7**, e006428 (2018).
36. W. Feng *et al.*, *Circulation* **141**, 940–942 (2020).
37. W. T. Stockdale *et al.*, *Cell Rep.* **25**, 1997–2007.e7 (2018).
38. X. K. Qu *et al.*, *Mol. Med. Rep.* **12**, 3718–3724 (2015).
39. M. J. Brody *et al.*, *PLOS ONE* **7**, e51621 (2012).
40. E. Giacomelli *et al.*, *Cell Stem Cell* **26**, 862–879.e11 (2020).
41. F. Hofmann, V. Flockerzi, S. Kahl, J. W. Wegener, *Physiol. Rev.* **94**, 303–326 (2014).
42. M. J. Brody *et al.*, *Am. J. Physiol. Heart Circ. Physiol.* **310**, H269–H278 (2016).
43. K. H. Kim, T. G. Kim, B. K. Micales, G. E. Lyons, Y. Lee, *Dev. Dyn.* **236**, 2225–2234 (2007).
44. W. Huang, R. Zhang, X. Xu, *Dev. Biol.* **331**, 237–249 (2009).
45. Y. Han *et al.*, *Dev. Cell* **48**, 853–863.e5 (2019).
46. M. Ogawa *et al.*, *Science* **372**, 201–205 (2021).

ACKNOWLEDGMENTS

We thank D. Ward-van Oostwaard (LUMC) for assistance with hiPSC-CM experiments; B. de Jonge (AMC) for assistance in zebrafish isolation for patch-clamp experiments; D. Verteg (Hubrecht Institute) and E. van Rooij (Hubrecht Institute) for performing the original mouse MI procedures; D. Y. R. Stainier (MPI Bad Nauheim) and M. Mommersteeg (University of Oxford) for sending zebrafish lines; K. D. Poss (Duke University) for sending plasmids; J. Stein (LUMC) for providing the SoTa tool for sarcomere analysis; M. Dias Brescia (LUMC) and K. Barnes (Sartorius) for input into the real-time imaging and Sartorius for use of the Incucyte Live-Cell Analysis System; S. L. Kloet, E. de Meijer, and R. Menafr (Leiden Genome Technology Center) for help with 10X Genomics scRNA-seq (advice, library preparation, primary data alignment, and quality control); and F. Tessadori (Hubrecht Institute) for critical review of the manuscript. **Funding:** This study received support from an EMBO Long Term Fellowship ALTF1129-2015 (P.D.N.); an HFSPO Fellowship (LT001404/2017-L) (P.D.N.); NWO-ZonMW Veni grant (016.186.017-3) (P.D.N.); European Union's Horizon 2020 Research and Innovation Programme under the Marie Skłodowska-Curie action (MSCA-IF 838985 SIGNATURE) (G.C.); Netherlands Organ-on-Chip Initiative, an NWO Gravitation project funded by the Ministry of Education, Culture and Science of the government of the Netherlands (024.003.001) (C.L.M.); the European Research Council (ERC-CoG Mini-HEART no. 101001746) (M.Be.); the Novo Nordisk Foundation Center for Stem Cell Medicine supported by Novo Nordisk Foundation grants (NNF21CC0073729) (C.L.M.); the European

Research Council (ERC-StG IniReg 716894) (K.B.); the Netherlands Cardiovascular Research Initiative, an initiative with support of the Dutch Heart Foundation and Hartekind (CVON2019-002 OUTREACH) (J.B.); and NWO-ZonMW Open competition grant (CONTRACT 09120012010018) (J.B.). **Author contributions:** Conceptualization: P.D.N. and J.B. Investigation: P.D.N., G.C., I.G., A.O.V., H.H., M.Be., D.E.M.d.B., T.K., A.V., G.E.M.L., A.S., J.M., A.A.M., S.C., and T.P.d.B. Funding acquisition: P.D.N., K.B., E.T., C.L.M., M.Be., and J.B. Supervision: P.D.N., K.B., E.T., C.L.M., M.Be., and J.B. Writing – original draft: P.D.N. and J.B. Writing – review & editing: all authors. **Competing interests:** The authors declare that they have no competing interests. **Data and materials availability:** All data are available in the main text or the supplementary materials. Sequencing datasets can be accessed in GSE224156. The hiPSC line LUMC002iCTRL-06 (<https://hpscrg.eu/cell-line/LUMC028-A>) is available from M.Be. (Anatomy and Embryology Department) or C. Freund (iPSC core facility) under a material transfer agreement with Leiden University Medical Center. **License information:** Copyright © 2023 the authors, some rights reserved; exclusive licensee American Association for the Advancement of Science. No claim to original US government works. <https://www.science.org/about/science-licenses-journal-article-reuse>

SUPPLEMENTARY MATERIALS

[science.org/doi/10.1126/science.abo6718](https://doi.org/10.1126/science.abo6718)
Materials and Methods
Figs. S1 to S16
Table S1
References (47–72)
MDAR Reproducibility Checklist

[View/request a protocol for this paper from Bio-protocol.](#)

Submitted 24 February 2022; resubmitted 26 January 2023
Accepted 20 April 2023
10.1126/science.abo6718